LA-UR-18-30333 (Accepted Manuscript)

Investigating the Effect of the Closure in Partially-Averaged Navier–Stokes Equations

Soares Pereira, Filipe Miguel
Eca, Luis
Vaz, Guilherme

To be published in: Journal of Fluids Engineering

DOI to publisher's version: 10.1115/1.4043539

Permalink to record: http://permalink.lanl.gov/object/view?what=info:lanl-repo/lareport/LA-UR-18-30333

Investigating the Effect of the Closure in Partially-Averaged Navier-Stokes Equations

Filipe S. Pereira*
Postdoc Researcher
X-Computational Physics Division
Los Alamos National Laboratory
Los Alamos, New Mexico 87544
Email: fspereira@lanl.gov

Luís Eça
Assistant Professor
Mechanical Engineering Department
Instituto Superior Técnico
Lisbon, Portugal
Email: luis.eca@ist.utl.pt

Guilherme Vaz
Senior Researcher
R&D Department
Maritime Research Institute Netherlands
Wageningen, The Netherlands
Email: g.vaz@marin.nl

ABSTRACT

The importance of the turbulence closure to the modeling accuracy of the Partially-Averaged Navier-Stokes equations (PANS) is investigated in prediction of the flow around a circular cylinder at Reynolds number of 3900. A series of PANS calculations at various degrees of physical resolution is conducted using three Reynolds-Averaged Navier-Stokes equations (RANS) based closures: the standard, SST, and TNT $k-\omega$ models. The latter is proposed in this work. The results illustrate the dependence of PANS on the closure. At coarse physical resolutions, a narrower range of scales is resolved so that the influence of the closure on the simulations accuracy increases significantly. Among all closures, PANS-TNT achieves the lowest comparison errors. The reduced sensitivity of this closure to freestream turbulence quantities and the absence of auxiliary functions from its governing equations are certainly contributing to this result. It is demonstrated

*Address all correspondence related to ASME style format and figures to this author.

that the use of partial turbulence quantities in such auxiliary functions calibrated for total turbulent (RANS) quantities affects their behavior. On the other hand, the successive increase of physical resolution reduces the relevance of the closure, causing the convergence of the three models toward the same solution. This outcome is achieved once the physical resolution and closure guarantee the precise replication of the spatial development of the key coherent structures of the flow.

1 INTRODUCTION

The prediction of practical flows with Scale-Resolving Simulation (SRS) methods is a challenging area of computational fluid dynamics which has experienced a significant growth in the past two decades. Along with advances in computing power, the main contributor to its increasing popularity has been the development of multiple hybrid and bridging methods. Originally proposed by Speziale [1] and Spalart et al. [2], the former modeling strategies are intended to fill in the spectral gap between the Reynolds-Averaged Navier-Stokes equations (RANS) and Large-Eddy Simulation (LES) models, and overcome many of their inherent limitations. These typically range from the inadequacy of one-point RANS closures to represent complex flow phenomena such as massive flow separation or coherent structures, to the demanding numerical requisites of LES in computation of wall-bounded flows of engineering relevance [3, 4]

Despite sharing the same primary objective, hybrid and bringing strategies are based on distinct modeling concepts. Hybrid models combine RANS in attached boundary-layers with a SRS formulation in the remainder turbulent flow regions. In this manner, the numerical demands are relaxed in comparison to LES, and the representation of detached and massively separated flow areas enhanced. Bridging formulations, on the other hand, operate at any degree of physical resolution (range of resolved scales) using a single mathematical model in the entire computational domain. Additionally, this class of SRS methods can be applied at constant physical resolution which enables the separate assessment of numerical and modeling errors and prevents commutation errors [5, 6]. These arise from the fact that SRS formulations at variable physical resolution do not guarantee the scale-invariance property of the Navier-Stokes equations [7] since the filtering operator no longer commutes in space and time with differentiation, *i.e.* $\langle \frac{\partial \Phi}{\partial x_j} \rangle \neq \frac{\partial \langle \Phi \rangle}{\partial x_j}$ and $\langle \frac{\partial \Phi}{\partial t} \rangle \neq \frac{\partial \langle \Phi \rangle}{\partial t}$. In both modeling strategies, the effect of the unresolved turbulent scales in the resolved field is commonly represented through a constitutive relation based on a RANS closure. Detached-Eddy Simulation (DES) [2], Delayed Detached-Eddy Simulation (DDES) [8], Partially-Averaged Navier-Stokes equations (PANS) [9–11], and Partially-Integrated Transport Model (PITM) [12] are examples of prominent hybrid and bridging methods, respectively.

The modeling accuracy of hybrid and bridging models is determined by two major aspects: *i)*

the selected degree of physical resolution; and *ii)* the quality of the closure model representing the unresolved turbulent scales. The first, determines the range of resolved scales and so it is expected that increasing the physical resolution improves the predictions accuracy at the expense of larger numerical requisites - grid (spatio-temporal) resolution, iterative convergence criterion, and sampling time to converge the flow statistics. As observed in Pereira et al. [13, 14], the physical resolution should guarantee that most of the coherent field [15, 16] is resolved and that only fully-developed turbulence is modeled. The second, dictates the accuracy of the modeling of the unresolved scales. Therefore, an enhancement in the closure quality may obviate the numerical requisites of the simulations by reducing the necessary degree of physical resolution to achieve an intended modeling accuracy. This, in turn, depends on the flow problem, application, and quantities of interest. In cases of computations at variable physical resolution, the magnitude of the commutation error is an additional factor contributing to the overall quality of the SRS computations [5].

The objective of this investigation is to evaluate the relevance of the closure model to the modeling accuracy of PANS, along with its dependence on the physical resolution. Toward this end, a series of PANS computations is performed with three $k-\omega$ closures at distinct degrees of physical resolution. A new PANS closure is proposed which is expected to achieve an enhanced accuracy at reduced physical resolutions. The selected test case is the flow around a circular cylinder at Reynolds number of $Re = 3900$. Despite the reduced Reynolds number, this problem provides a challenging, experimentally well documented, and affordable[1] case to initiate the building of the validation space [17, 18] of the new PANS closure. Note that the former features made this flow problem a reference validation case for turbulence modeling [19–28]. The effects of the commutation error are not addressed in this study and so all simulations are conducted at constant physical resolution. The physical rationale of the results is interpreted using the findings and conditions of Pereira et al. [13, 14].

The remainder of the article is structured as follows. Section 2 describes the three PANS closures evaluated in this study. The derivation of the new PANS closure is provided in Appendix A. The details of the flow problem and simulations are then introduced in Section 3. Thereafter,

[1] numerical requisites to attain adequate numerical errors, ideally below the modeling error.

Section 4 discusses the results, whereas Section 5 concludes the investigation with a summary of its findings.

2 PARTIALLY-AVERAGED NAVIER-STOKES EQUATIONS

Consider an arbitrary filtering operator commuting with differentiation and constant preserving which decomposes any given flow quantity Φ into a resolved $\langle\Phi\rangle$ and modeled ϕ component,

$$\Phi = \langle\Phi\rangle + \phi \ . \tag{1}$$

From the scale invariance property [7, 9], the application of such operator to the Navier-Stokes equations leads to the Partially-Averaged Navier-Stokes equations (PANS) [9–11],

$$\frac{\partial\langle V_i\rangle}{\partial x_i} = 0 \ , \tag{2}$$

$$\frac{D\langle V_i\rangle}{Dt} = -\frac{1}{\rho}\frac{\partial\langle P\rangle}{\partial x_i} + \frac{\partial}{\partial x_j}\left[\nu\left(\frac{\partial\langle V_i\rangle}{\partial x_j} + \frac{\partial\langle V_j\rangle}{\partial x_i}\right)\right] + \frac{1}{\rho}\frac{\partial\tau_{ij}(V_i,V_j)}{\partial x_j} \ , \tag{3}$$

where x_i are the coordinates of a Cartesian coordinate system, V_i are the Cartesian velocity components, P is the pressure, ρ is the fluid density, ν is the kinematic viscosity, and $\tau_{ij}(V_i,V_j)$ is the generalized central second moment [7] that represents the effect of the modeled turbulent scales into the resolved flow field. Note that equations 2 and 3 assume incompressible and single-phase fluid. However, the previous system of equations is not closed due to $\tau_{ij}(V_i,V_j)$. This quantity is here modeled through the Boussinesq hypothesis,

$$\frac{\tau_{ij}(V_i,V_j)}{\rho} = 2\nu_t\langle S_{ij}\rangle - \frac{2}{3}k\delta_{ij} \ , \tag{4}$$

being ν_t the turbulent viscosity, $\langle S_{ij} \rangle$ the resolved strain-rate tensor, k the modeled turbulence kinetic energy, and δ_{ij} the Kronecker symbol. The relation of equation 4 creates two additional unknowns (k and ν_t) which require further modeling. Such variables are calculated in this work using three distinct $k-\omega$ closures.

PANS closures [9] are traditionally based on existent one-point RANS models. Two parameters are introduced in the governing equations of the RANS closure to determine the fraction of the turbulence quantities being modeled. For the case of $k-\omega$ closures, these are the modeled-to-total ratio of turbulence kinetic energy f_k and specific dissipation rate f_ω,

$$f_k \equiv \frac{k}{k_T}, \qquad f_\omega \equiv \frac{\omega}{\omega_T} = \frac{f_\epsilon}{f_k}. \tag{5}$$

In the previous relations, the subscript T denotes total quantities (instead of a capital symbol, equation 1), ω is the specific dissipation rate, and f_ϵ the modeled-to-total ratio of turbulence dissipation $\epsilon \propto \omega k$. The closures used in this investigation are based on the $k-\omega$ of Wilcox (WX) [29], the $k-\omega$ Shear-Stress Transport (SST) of Menter et al. [30], and the $k-\omega$ Turbulent/Non-Turbulent (TNT) of Kok [31]. The resultant PANS closures possess the following general form for the transport equations of k and ω,

$$\frac{Dk}{Dt} = P_k - \beta^* \omega k + \frac{\partial}{\partial x_j}\left[\left(\nu + \nu_t \sigma_k \frac{f_\omega}{f_k}\right)\frac{\partial k}{\partial x_j}\right] , \tag{6}$$

$$\frac{D\omega}{Dt} = \frac{\alpha}{\nu_t} P_k - \left(P' - \frac{P'}{f_\omega} + \frac{\beta\omega}{f_\omega}\right)\omega + \frac{\partial}{\partial x_j}\left[\left(\nu + \nu_t \sigma_\omega \frac{f_\omega}{f_k}\right)\frac{\partial \omega}{\partial x_j}\right] + D_c \, , \tag{7}$$

where $P' = \alpha\beta^* k/\nu_t$, $P_k = \nu_t \langle S \rangle^2$ is the production of turbulence kinetic energy, $\langle S \rangle$ is the magnitude of $\langle S_{ij} \rangle$, D_c is the cross-diffusion term, and α, β, β^*, σ_k, and σ_ω are coefficients. The

differences between closures lie in the cross-diffusion term, the manner how the turbulent viscosity is calculated, and evidently the coefficients. These features are described below and in Tab. 1. The complete derivation of such PANS closures is presented in Appendix A.

2.1 $k-\omega$ Closure

The $k-\omega$ closure of Wilcox (WX) [29] has been widely used in diverse areas of engineering due to its robustness and ability to accurately predict wall-bounded flows with moderate adverse pressure gradients. For this reason, Lakshmipathy and Girimaji [32] adapted such model to PANS. In this PANS closure, the modeled turbulence kinetic energy k and specific dissipation rate ω are calculated from equations 6 and 7 with the cross-diffusion term being equal to zero, $D_c = 0$. The turbulent viscosity, on the other hand, is defined as

$$\nu_t = \frac{k}{\omega} \, . \tag{8}$$

2.2 $k-\omega$ SST Closure

Despite its advantages, the WX closure exhibits a strong sensitivity to the freestream values specified for the dependent turbulence quantities (in particular, ω), and it is inadequate predicting flows characterized by separation on continuous surfaces. Consequently, Menter [33,34] proposed the $k-\omega$ SST model to enhance the response of the standard $k-\omega$ model to the former issues. To accomplish such objective, the SST combines the $k-\omega$ (WX) in the near-wall region with the $k-\epsilon$ in outer regions. An additional term named cross-diffusion is therefore added to the ω transport equation of the WX model in order to combine the WX and $k-\epsilon$ closures. In the PANS form proposed by Pereira et al. [35], this term is defined as

$$D_c = 2\frac{\sigma_{\omega_2}}{\omega}\frac{f_\omega}{f_k}\left(1-F_1\right)\frac{\partial k}{\partial x_j}\frac{\partial \omega}{\partial x_j} \, , \tag{9}$$

where σ_{ω_2} is a coefficient [30], F_1 is an auxiliary function ($0 \leq F_1 \leq 1$),

$$F_1 = \tanh\left(\min\left\{\max\left\{\frac{\sqrt{k}}{\beta^*\omega d}; \frac{500\nu}{d^2\omega}\right\}; \frac{4\rho\sigma_{\omega_2}k}{d^2\max\left\{\frac{2\rho\sigma_{\omega_2}}{\omega}\frac{\partial k}{\partial x_j}\frac{\partial \omega}{\partial x_j}; 10^{-10}\right\}}\right\}^4\right), \tag{10}$$

and d is the nearest wall distance. The coefficients α, β, σ_k and σ_ω of the SST closure are computed from

$$\Phi = \Phi_1 F_1 + \Phi_2\left(1.0 - F_1\right), \tag{11}$$

being Φ a given coefficient with the indexes 1 and 2 denoting its WX and $k-\epsilon$ values, respectively. Finally, the magnitude of the Reynolds-stress tensor is limited in severe adverse pressure gradient flows through the following expression for the turbulent viscosity,

$$\nu_t = \frac{a_1 k}{\max\left\{a_1\omega; \langle S\rangle F_2\right\}}, \tag{12}$$

where a_1 is a coefficient, and F_2 is a second auxiliary function ($0 \leq F_2 \leq 1$) defined as

$$F_2 = \tanh\left(\max\left\{\frac{2\sqrt{k}}{\beta^*\omega d}; \frac{500\nu}{d^2\omega}\right\}^2\right). \tag{13}$$

The SST coefficients used in this work are those given in Menter et al. [30].

2.3 $k-\omega$ TNT Closure

The SST closure has been widely and successfully used in RANS, motivating its adaptation to various SRS formulations (see for instance Gritskevich et al. [36] or Pereira et al. [35]). Its governing equations use two auxiliary functions (F_1 and F_2) which are calibrated for total turbulence

quantities ($f_k = 1.00$). However, the estimation of total turbulence quantities is troublesome in SRS computations of statistically unsteady flows[2] with coherent structures [37]. Consequently, such auxiliary functions are commonly computed with the dependent quantities of the closure which only consider the portion of the turbulence field being modeled. This option may lead to a deficit in their performance, particularly relevant at reduced physical resolutions. This aspect is addressed later in Section 4.2.1.

The TNT closure of Kok [31] is an alternative formulation to reduce the sensitivity of the WX to freestream turbulence conditions that does not require auxiliary functions (nor the wall distance). Toward this end, the contribution of the cross-diffusion term is simply defined by the sign of the product between the gradient of the turbulence kinetic energy and specific dissipation rate. As a result, in PANS-TNT the cross-diffusion term is calculated without any ambiguity as follows,

$$D_c = \frac{f_\omega}{f_k}\frac{\sigma_d}{\omega}\max\left\{\frac{\partial k}{\partial x_j}\frac{\partial \omega}{\partial x_j};0\right\} \ . \tag{14}$$

The turbulent viscosity is calculated from equation 8.

3 FLOW PROBLEM AND SIMULATIONS DETAILS

3.1 Flow Problem

The test case evaluated in this investigation is the flow around a circular cylinder at Reynolds number Re based on the freestream velocity V_∞ and cylinder diameter D equal to 3900. This Reynolds number places the flow in the regime where turbulent transition occurs in the free shear-layer [38] - $3.5 \times 10^2 \leq Re \leq 2.0 \times 10^5$. For this reason, the flow exhibits a laminar boundary-layer, separation, and free shear-layer; turbulence onset; turbulent free shear-layer and wake. Furthermore, this problem entails two coherent structures that govern the flow physics in the free shear-layers. These are the Kelvin-Helmholtz (KH) and vortex-shedding (VS) structures. Yet, the first can only be reliably observed in experiments for Reynolds numbers exceeding 1200 [39].

The present flow problem has been experimentally studied by Ong and Wallace [40], and Par-

[2]flows with a time dependent mean-flow field.

naudeau et al. [41]. The results of the latter experimental study are used in this investigation to estimate the comparison error in predictions of the Strouhal number St and the time-averaged velocity field - streamwise magnitude $\langle\overline{V_1}\rangle$ and covariance $\overline{v_1 v_2}$. Although at slightly different experimental conditions, the measurements of Norberg [42, 43] are also used as reference data for the time-averaged pressure coefficient on the cylinder surface $\overline{C}_p(\theta)$ and resulting functional quantities.

3.2 Simulations Details

The computations are performed with the community based open-usage solver ReFRESCO [44]. The closed set of governing equations described in Section 2 is discretized using a finite-volume approach with cell-centered collocated variables and in strong conservation form. A pressure-correction equation based on the SIMPLE algorithm is used to ensure mass conservation. Both spatial and temporal discretization schemes are second-order accurate. At each implicit time-step, the non-linear system for velocity and pressure is linearised with Picard's method, and a segregated approach is adopted here for the solution of all transport equations. The simulations are run in parallel using MPI and subdomain decomposition.

The computational domain used in the calculations is a rectangular prism centered at the cylinder axis with dimensions in the streamwise x_1, transverse x_2, and spanwise x_3 directions of $50D \times 24D \times 3D$, respectively. At the inlet boundary, $x_1/D = -10$, the velocity and turbulent quantities are set constant while the pressure is extrapolated from the interior of the domain. The turbulence kinetic energy and specific dissipation rate are defined from a turbulence intensity of $I = 0.2\%$ [41], and $\nu_t/\nu = 10^{-3}$. On the other hand, at the outlet boundary, $x_1/D = 40$, the streamwise derivatives of all dependent variables are set equal to zero. No-slip and impermeability conditions are prescribed on the cylinder, whereas the normal pressure derivative is set equal to zero. Furthermore, the turbulence kinetic energy is set equal to zero, and the specific dissipation rate is calculated as $\omega = f_\omega 80\nu d^{-2}$ (adapted from Wilcox [45]). At the top and bottom boundaries, $x_2/D = \pm 12$, the pressure is imposed and the transverse derivatives of the remainder dependent variables are equal to zero. Symmetry boundary conditions are applied at the lateral boundaries, $x_3/D = 0$ and 3. This option stems from the fact that neither cyclic nor symmetry conditions are

optimal to deal with the spanwise wavelengths of the coherent field [46]. A detailed description of the simulations can be found in Pereira et al. [28].

All calculations are conducted on a grid with $4,546,800$ cells and a time-step of 5.209×10^{-3} time-units tV_∞/D. The selection of this grid stems from the verification exercises performed in Pereira et al. [28] which illustrate its adequacy (reduced numerical uncertainty) for this problem and mathematical models. The simulations run for 500 time-units and start from an initial RANS computation of 200 time-units. All the analyzed flow statistics are then computed with a minimum of 350 time-units. In order to minimize round-off and iterative errors, the computations are conducted on double precision with an iterative convergence criterion that requires a maximum normalized residual of 10^{-5} for all dependent variables and time instants. This leads to an averaged number of iterations per time instant varying from 21 to 55 with the reduction of f_k. Four distinct values of f_k are used in this work: 1.00, 0.75, 0.50, and 0.25. In the case of PANS-SST, $f_k = 0.15$ is also used. On the other hand, f_ϵ is set equal to unity since it is assumed that all turbulence dissipation occurs in the modeled scales. In this manner, the physical resolution of the mathematical model is determined by f_k, and $f_\omega = f_k^{-1}$.

4 RESULTS

The results of this investigation are discussed in this section. It starts by comparing the modeling accuracy of the different PANS closures in the prediction of the selected flow problem - Section 4.1. This is accomplished by evaluating the comparison error $E_c(\Phi)$ defined as the difference between the numerical result and the experimental measurement. Thereafter, the outcome is discussed in Section 4.2 through the examination of the auxiliary functions and cross-diffusion term of the PANS closures, along with the physics of the results. Note that all the selected flow quantities are made dimensionless using V_∞, D, and ρ.

4.1 Closures Comparison

A series of computations with the distinct PANS closures have been performed at successive finer degrees of physical resolution ($f_k \to 0$) to investigate the relevance of these aspects to the modeling error. Functional and local flow quantities are measured and compared against the

experiments of Parnaudeau et al. [41] and Norberg [42,43]. These are defined as in the reference experiments [41–43]. The outcome is presented in Tab. 2, and Figs. 1 to 3.

Table 2 shows the predictions and respective comparison error for the time-averaged drag coefficient $\overline{C}_D$, root-mean-square lift coefficient C'_L, time-averaged pressure base coefficient $\overline{C}_{pb}$, Strouhal number St, and flow recirculation length $\overline{L}_r$ measured at $x_2/D = 0$. The results of the Strouhal number indicate that the frequency of vortex-shedding is accurately predicted by all closures even when all flow scales are modeled ($f_k = 1.00$). The comparison error does not exceed 2.8% of the experimental measurement for all cases. On the other hand, the influence of the closure is significantly larger for the force and pressure coefficients - $\overline{C}_D$, C'_L, and $\overline{C}_{pb}$. In this case, the discrepancies between simulations at $f_k = 1.00$ and experiments reach 27.7% for $\overline{C}_D$, 591.8% for C'_L, and 59.7% for $\overline{C}_{pb}$. Comparing all closures, the SST leads to the largest mismatches with the experimental measurements which may exceed in 32% those obtained for the WX or TNT. Overall, the outcome of computations at $f_k = 1.00$ illustrates the inadequacy of the closures to represent all scales of this flow problem, *i.e.* to operate in the framework of RANS.

Nonetheless, the successive increase of physical resolution ($f_k \to 0$) leads to a substantial enhancement of the predictions quality. For instance, $E_c(C'_L)$ reduces from 474.1% to 2.7% when the physical resolution in PANS-TNT computations is refined from $f_k = 1.00$ to 0.25. The data also exhibit three clear tendencies upon the reduction of f_k: *i)* the comparison error tends to diminish for all closures and analyzed quantities; *ii)* as the range of resolved scales increases, the relevance of the closure decreases so that all models start converging toward the same solution. This is illustrated in Fig. 1 for PANS-TNT at $f_k \leq 0.50$ while for the remainder models at $f_k < 0.50$. Such outcome points out the existence of a combination of closure and physical resolution for which the advantages of further increasing the physical resolution are reduced [13,28]; and *iii)* at coarse physical resolutions the importance of the closure increases significantly. Most notably, PANS-SST exhibits an apparent deterioration of the predictions accuracy ($E_c(\Phi)$) between $f_k = 1.00$ and 0.75. The reasoning for this result is addressed later.

The former tendencies are also observed for the predictions of the flow recirculation length. Yet, the results are converging toward a larger recirculation length than that measured experimen-

tally. As shown in Pereira et al. [13, 28, 47] and Breuer [48], this is certainly a consequence of the specification of time-averaged boundary conditions at the inlet of the domain which causes a later onset of turbulence [49].

Similar conclusions can be inferred for the time-averaged pressure coefficient on the cylinder surface $\overline{C}_p(\theta)$, and the streamwise magnitude $\langle\overline{V_1}\rangle$ and covariance $\overline{v_1 v_2}$ velocity fields in the near-wake - Figs. 2 and 3. The magnitude of the pressure coefficient is overpredicted by all closures at coarse physical resolutions ($f_k > 0.50$). In fact, it is even visible that the inadequacy of the models to predict the flow at $f_k > 0.50$ is affecting the attached laminar boundary-layer by reducing its thickness. This leads to larger values of $\overline{C}_p$ for $\theta < 90^o$ than those measured in the experiments. Nonetheless, the increase of physical resolution enhances the quality of the solutions, and at $f_k = 0.25$ the comparison error is negligible for all closures. It is also interesting to observe that once again PANS-SST leads to the largest comparison errors, while for PANS-TNT the differences between simulations using $f_k \leq 0.50$ are small.

Referring to the velocity profiles of Fig. 3, the data illustrate a lower velocity deficit in the near-wake at coarse physical resolutions which leads to a V-shape profile. As f_k decreases, these profiles start exhibiting a U-shape similar to the experiments. Consequently, the comparison error is reduced. On the other hand, the covariance velocity profiles (or specific shear stress) is clearly overpredicted at $f_k \geq 0.50$. The exception is PANS-TNT at $f_k = 0.50$ which points out the enhanced ability of this closure to predict this flow problem. At $f_k = 0.25$, all simulations are in very good agreement with the experiments.

In summary, the results have shown the following: *i)* the simulations converge toward the same solution once a given set of closure and physical resolution is achieved; *ii)* the predictions are in good agreement with the experiments (and available DNS data [24]) for $f_k \leq 0.50$; *iii)* PANS-TNT leads to lower comparison errors than the remainder closures; and *iv)* computations at coarse physical resolutions ($f_k > 0.50$) may exhibit larger comparison errors than at $f_k = 1.00$. The modeling and physical reasoning for these outcomes is now discussed.

4.2 Modeling And Physical Interpretation

4.2.1 Auxiliary Functions and Cross-Diffusion Term

The modeling accuracy of a SRS method is closely dependent on the physical resolution. As a wider range of flow scales is resolved, the turbulence closure has a diminishing relevance to the overall modeling accuracy. Furthermore, the scales being modeled are more likely to fulfill the envelope of the closure since they are less dependent on boundary conditions and the coherent field. It is therefore expected that increasing the physical resolution enhances the quality of the predictions. However, the results of this investigation have shown a general deficit in the performance of PANS-SST when the physical resolution is refined from $f_k = 1.00$ (RANS) to 0.75. Note that this outcome cannot be uniquely explained by possible disturbances resulting from numerical errors.

As discussed in Section 2, one of the specificities of the SST closure is the use of the auxiliary functions F_1 and F_2. These determine the flow regions where *i)* the WX and $k-\epsilon$ closures (equation 9) are active - F_1; and *ii)* the turbulent viscosity (equation 12) is limited by $a_1 k/\langle S \rangle$ - F_2. Such functions are defined by equations 10 and 13, and entail the use of total turbulence quantities. However, whereas the dependent variables of a RANS ($f_k = 1.00$) closure are total turbulence quantities, those calculated in SRS computations only represent the portion of the turbulence field being modeled by the closure. This feature turns the calculation of total turbulence quantities in SRS complex for statistically unsteady flows with coherent structures, in particular during simulations. For this reason, partial turbulence quantities are commonly used in SRS models [35, 36].

To investigate the importance of this option and explain the consequences to the accuracy of PANS-SST, the parameters f_k and f_ω (for $f_\epsilon = 1.00$, $f_\omega = f_k^{-1}$) are included in equations 10 and 13 so that all turbulence variables are total quantities.

$$F_1 = \tanh\left(\min\left\{\max\left\{\underbrace{f_k^{3/2}\frac{\sqrt{k_T}}{\beta^* \omega_T d}}_{T_1}; \underbrace{f_k \frac{500\nu}{d^2 \omega_T}}_{T_2}\right\}; \underbrace{\frac{4\rho\sigma_{\omega_2} k_T}{d^2 \max\left\{\frac{2\rho\sigma_{\omega_2}}{\omega_T}\frac{\partial k_T}{\partial x_j}\frac{\partial \omega_T}{\partial x_j}; 10^{-10}\right\}}}_{T_3}\right\}^4\right), \quad (15)$$

$$F_2 = \tanh\left(\max\left\{\underbrace{f_k^{3/2}\frac{2\sqrt{k_T}}{\beta^*\omega_T d}}_{2T_1}; \underbrace{f_k\frac{500\nu}{d^2\omega_T}}_{T_2}\right\}^2\right) . \tag{16}$$

The first and most significant consequence of using partial quantities to determine F_1 and F_2 is that the terms T_1 and T_2 tend to zero upon the reduction of f_k. Moreover, this tendency occurs at different rates: T_1 decreases with $f_k^{3/2}$, whereas T_2 with f_k. On the other hand, the third term T_3 is not directly affected by f_k. Nonetheless, the gradients of the turbulence kinetic energy and specific dissipation rate may increase with the physical resolution due to the inherent larger irregularity of the resolved turbulent field.

Such simple analysis has demonstrated that the reduction of f_k will certainly affect the calibration of the two auxiliary functions when used in SRS models. It shows that as the physical resolution increases ($f_k \rightarrow 0$), the auxiliary functions F_1 and F_2 converge to zero. This makes the SST model to apply the standard $k-\epsilon$ closure successively closer to the near-wall region, and reduces the area where the turbulent viscosity can be limited by $a_1 k/\langle S\rangle$. It is important to highlight again that the standard $k-\epsilon$ is not intended to operate in the near-wall region.

We now examine the effects of these aspects to the predictions of the present flow problem. Toward this end, Fig. 4 depicts the variation of the time-averaged auxiliary functions $\overline{F}_1$ and $\overline{F}_2$ with f_k. Similarly to the conclusions drawn in the analysis of equations 15 and 16, the results indicate that the area where $\overline{F}_1$ and $\overline{F}_2$ are equal to one reduces with the physical resolution. In this manner, the region where WX is applied diminishes. However, in this case, at $f_k \leq 0.25$ such variation decelerates. This might be related with differences in the flow physics caused by the physical resolution (see Section 4.2.2).

Finally, Fig. 5 compares the time-averaged ratio of the cross-diffusion and production terms $\overline{D}_c/\overline{P}_\omega$ obtained from PANS computations using the SST and TNT closures at various degrees of physical resolution. Apart from differences in the magnitude of $\overline{D}_c/\overline{P}_\omega$, the results for PANS-SST using $f_k < 1.00$ indicate that the variations in $\overline{F}_1$ lead to negative values of $\overline{D}_c/\overline{P}_\omega$ in the region $x_1/D \leq 0.64$. Note that the criterion used in the TNT closure to activate the cross-diffusion term guarantees $D_c/P_\omega \geq 0$ - Fig. 5b. For the present flow and PANS-SST closure, this is only observed

at $f_k = 1.00$.

Overall, the resulting negative values of $\overline{D}_c/\overline{P}_\omega$ suggest that the use of partial turbulence quantities leads to a significant change of behavior of the auxiliary functions that affects the accuracy of PANS-SST. As a result of the absence of auxiliary functions in its governing equations, PANS-TNT does not experience such issues. We believe this explains its superior performance at coarse physical resolutions in comparison to PANS-SST.

4.2.2 Physical Rationale

The flow around a circular cylinder in the regime where turbulent transition occurs in the free shear-layer is dominated by two coherent structures [13,14]. These are the Kelvin-Helmholtz (KH) and vortex-shedding (VS) structures. Their spatial development comprises four key stages: *i)* the onset of the KH instability in the free shear-layer; *ii)* the spatial development of the KH rollers; *iii)* breakdown to high intensity turbulence; and *iv)* roll-up of the turbulent free shear-layer leading to vortex-shedding. In addition, it has been demonstrated that the precise replication of the previous stages requires an effective computational Reynolds number Re_e,

$$Re_e \equiv \frac{V_\infty D}{\nu + \nu_t} \, , \tag{17}$$

larger than 1200. This is the lowest Re to experimentally observe the KH rollers [39]. Along with $Re_e \geq 1200$, the mean-to-unresolved strain-rate ratio $\langle S \rangle k/\epsilon$ should be inferior to 6 in order to guarantee that only fully-developed turbulence is represented by the closure. The former findings and conditions are now used to explain the observed differences in modeling accuracy upon closure and physical resolution. The results for the time-averaged effective computational Reynolds number and mean-to-unresolved strain-rate ratio are depicted in Figs. 6 and 7. In both figures, the inflection line $\partial^2 \langle \overline{V_1} \rangle / \partial x_2^2$ representing the free shear-layer is also plotted.

The values of Re_e presented in Fig. 6 indicate that at coarse physical resolutions ($f_k > 0.50$) the effective computational Reynolds number is lower than 1200 in almost the entire free shear-layer. As discussed in Pereira et al. [13], one-point closures are not intended to represent the

coherent field and so tend to overpredict turbulence in those regions - Fig. 7. Consequently, Re_e is excessively reduced which causes the inaccurate representation of the spatial development of the KH and vortex-shedding structures. Note that the inward curving is initiated at approximately the point where the free shear-layer experiences an effective computational Reynolds number below 1200. Naturally, the refinement of the physical resolution increases Re_e. At $f_k = 0.50$, the effective computational Reynolds number is larger than 1200 in a significant portion of the free shear-layer. This is particularly visible for PANS-TNT, being the cause for the reduced comparison errors and the similarities with the case at $f_k = 0.25$. Furthermore, Fig. 7 show that $\langle S \rangle k/\epsilon$ does not exceed 6, indicating that the closure is mainly representing fully-developed turbulence. This suggests that most of the coherent field is being resolved. Finally, at $f_k = 0.25$ the free shear-layers predicted by all closures do not experience $Re_e < 1200$ nor $\langle S \rangle k/\epsilon > 6$. This indicates that the spatial development of the vortex-shedding is accurately represented, explaining the similarity between the predictions of the distinct closures.

The former results are evidently visible in the frequency spectra plotted in Fig. 8. Independently of the closure, computations at $f_k > 0.50$ are only capable of capturing the vortex-shedding frequency and its harmonics. This stems from the overproduction of turbulence which excessively decreases Re_e and diffuses the KH rollers. On the other hand, computations at $f_k = 0.50$ enable the mathematical models to enhance the replication of the spatial the development of the KH and vortex-shedding structures. For this reason, it is possible to visualize the characteristic broadband frequency of the KH rollers - Fig. 8c. The further increase of physical resolution leads to a significant reduction of the differences between the solutions of the three closures, and to remarkable similarities between the simulations and the experiments used as reference - Fig. 8e.

5 CONCLUSIONS

This investigation has analyzed the relevance of the turbulence closure to the modeling accuracy of PANS, along with the influence of the physical resolution f_k. Three PANS closures are compared in the prediction of the flow around a circular cylinder at $Re = 3900$. These are the WX of Lakshmipathy and Girimaji [32], the SST of Pereira et al. [35], and the TNT proposed here.

To accomplish the former objectives, a series of PANS computations is performed with the three closures at various degrees of physical resolution. The modeling accuracy of the predictions is then evaluated through the comparison error using the experiments of Parnaudeau et al. [41] and Norberg [42, 43] as reference. The modeling and physical rationale behind the results is also examined.

The results of the PANS computations at coarse physical resolutions ($f_k > 0.50$) have demonstrated that the three closures are inadequate to represent the physical phenomena exhibited in this flow. Nonetheless, the PANS-TNT closure exhibits the smallest discrepancies with the experiments. Furthermore, the predictions of PANS-SST show an apparent deterioration of the modeling accuracy at coarse physical resolutions which is not observed for the remainder PANS closures. Such outcome is certainly related to the use of partial turbulence quantities in the calculation of the auxiliary functions of the SST closure. This option stems from the difficulties to estimate total turbulence quantities during a simulation of a statistically unsteady flow with coherent structures. The proposed PANS-TNT overcomes such issue due to the absence of auxiliary functions in its governing equations. Hence, this closure is an attractive option for SRS strategies intended to operate at a wide range of physical resolutions and predict wall-bounded flows featured by flow separation.

The successive refinement of the physical resolution beyond a threshold value leads to a significant reduction of the differences between the solution of the three closures. This outcome is attained once the physical resolution and closure guarantee the accurate replication of the spatial development of KH and vortex-shedding coherent structures. The results also reiterate the validity of the two criteria proposed in Pereira et al. [13] for the accurate simulation of the present flow regime: an effective computational Reynolds number $Re_e \geq 1200$ and a mean-to-unresolved strain-rate ratio $\langle S \rangle k/\epsilon < 6$.

Overall, this investigation has highlighted the importance of the closure to the modeling accuracy of SRS formulations. The outcome indicates that accurate closures not requiring auxiliary functions or relations using total turbulence quantities can be advantageous for SRS methods. The proposed PANS-TNT seems to be an example of such formulations. In comparison to the

WX and SST closures, PANS-TNT reduces the physical resolution to achieve a given degree of modeling accuracy and so relaxes the numerical requirements of the simulations. For instance, it is observed an increase of 10% and 75% in the averaged number of iterations per time step to converge the computations when PANS-SST and PANS-WX at $f_k = 0.25$ are used instead of PANS-TNT at $f_k = 0.50$, respectively. Nonetheless, and despite the promising results, the establishment of PANS-TNT as an accurate and robust engineering tool requires further studies to expand its validation space.

ACKNOWLEDGEMENTS

The authors would like to thank the Maritime Research Laboratory Netherlands (MARIN) and the Laboratory for Advanced Computing at University of Coimbra for providing the HPC resources necessary to perform the present research.

REFERENCES

[1] Speziale, C., 1997. "Computing Non-Equilibrium Turbulent Flows With Time-Dependent RANS and VLES". In 15th International Conference on Numerical Methods in Fluid Dynamics, P. Kutler and J. F. J. Chattot, eds., Vol. 490 of *Lecture Notes in Physics*, Springer.

[2] Spalart, P., Jou, W.-H., Strelets, M., and Allmaras, S., 1997. "Comments on the Feasibility of LES for Wings, and on a Hybrid RANS/LES Approach". In Proceedings of the 1st Air Force Office of Scientific Research (AFOSR) International Conference on DNS/LES.

[3] Spalart, P., 2000. "Strategies for Turbulence Modelling and Simulations". *International Journal of Heat and Fluid Flow,* **21**(3), pp. 252–263.

[4] Davidson, P., 2004. *Turbulence: An Introduction for Scientists and Engineers*, first ed. Oxford University Press, New York, United States of America.

[5] Hamba, F., 2011. "Analysis of Filtered NavierStokes equation for Hybrid RANS/LES Simulation". *Physics of Fluids,* **23**(015108).

[6] Girimaji, S., and Wallin, S., 2013. "Closure Modeling in Bridging Regions of Variable-Resolution (VR) Turbulence Computations". *Journal of Turbulence,* **14**(1), pp. 72–98.

[7] Germano, M., 1992. "Turbulence: the Filtering Approach". *Journal of Fluid Mechanics,* **238**, pp. 325–336.

[8] Spalart, P., Deck, S., Shur, M., Squires, K., Strelets, M., and Travin, A., 2006. "A New Version of Detached-Eddy Simulation, Resistant to Ambiguous Grid Densities". *Theoretical and Computational Fluid Dynamics,* **20**, pp. 181–195.

[9] Girimaji, S., 2005. "Partially-Averaged Navier-Stokes Model for Turbulence: A Reynolds-Averaged Navier-Stokes to Direct Numerical Simulation Bridging Method". *Journal of Applied Mechanics,* **73**(3), pp. 413–421.

[10] Girimaji, S., Jeong, E., and Srinivasan, R., 2005. "Partially Averaged Navier-Stokes Method for Turbulence: Fixed Point Analysis and Comparison With Unsteady Partially Averaged Navier-Stokes". *Journal of Applied Mechanics,* **73**(3), pp. 422–429.

[11] Srinivasan, R., and Girimaji, S., 2014. "Partially-Averaged Navier-Stokes Simulations of High-Speed Mixing Environement". *Journal of Fluids Engineering,* **136**(6), 060903.

[12] Schiestel, R., and Dejoan, A., 2005. "Towards a New Partially Integrated Transport Model for Coarse Grid and Unsteady Turbulent Flow Simulations". *Theoretical and Computational Fluid Dynamics,* **18**(6), pp. 443–468.

[13] Pereira, F., Eça, L., Vaz, G., and Girimaji, S., 2018. "Challenges in Scale-Resolving Simulations of Turbulent Wake Flows with Coherent Structures". *Journal of Computational Physics,* **263**, pp. 98–115.

[14] Pereira, F., Eça, L., Vaz, G., and Girimaji, S., 2019. "On the Simulation of the Flow Around a Circular Cylinder at $Re = 140,000$". *International Journal of Heat and Fluid Flow,* **76**, pp. 40–56.

[15] Hussain, A., and Reynolds, W., 1970. "The Mechanics of an Organized Wave in Turbulent Shear Flow". *Journal of Fluid Mechanics,* **41**(2), pp. 241–258.

[16] Schiestel, R., 1987. "Multiple-Time-Scale Modeling of Turbulent Flows in One-Point Closures". *Physics of Fluids,* **30**, pp. 722–731.

[17] Trucano, T., Pilch, M., and Oberkampf, W., 2002. General Concepts for Experimental Validation of ASCI Code Applications. Technical Report SAND2002-0341, Sandia National Laboratories, Albuquerque, United States of America, March.

[18] Oberkampf, W., and Roy, C., 2010. *Verification and Validation in Scientific Computing*, first ed. Cambridge University Press, Cambridge, United Kingdom.

[19] Breuer, M., 1998. "Numerical and Modeling Influences on Large Eddy Simulations for the Flow Past a Circular Cylinder". *International Journal of Heat and Fluid Flow,* **19**(5), pp. 512–521.

[20] de With, G., and Holdø, A., 2005. "The Use of Solution Adaptive Grid for Modeling Small Scale Turbulent Structures". *Journal of Fluids Engineering,* **127**(5), pp. 936–944.

[21] Lakshmipathy, S., and Girimaji, S., 2010. "Partially-Averaged Navier-Stokes (PANS) Method for Turbulence Simulations: Flow Past a Circular Cylinder". *Journal of Fluids Engineering,* **132**(12), 121202.

[22] Lysenko, D., Ertesvåg, I., and Rian, K., 2012. "Large-Eddy Simulation of the Flow Over a Circular Cylinder at Reynolds Number 3900 Using the OpenFOAM Toolbox". *Flow, Turbulence*

and Combustion, **89**(4), pp. 491–518.

[23] Rosetti, G., Vaz, G., and Fujarra, A., 2012. "URANS Calculations for Smooth Circular Cylinder Flow in a Wide Range of Reynolds Numbers: Solution Verification and Validation". *Journal of Fluids Engineering,* **34**(12), 121103.

[24] Lehmkuhl, O., Rodríguez, I., Borrell, R., and Oliva, A., 2013. "Low-frequency Unsteadiness in the Vortex Formation Region of a Circular Cylinder". *Physics of Fluids,* **25**, 085109,.

[25] Sidebottom, W., Ooi, A., and Jones, D., 2015. "A Parametric Study of Turbulence Flow Past a Circular Cylinder Using Large Eddy Simulation". *Journal of Fluids Engineering,* **137**(9), 091202.

[26] Palkin, E., Mullyadzhanov, R., Hadžiabdić, M., and Hanjalić, K., 2015. "Scrutinizing URANS Models in Shedding Flows: the Case of Cylinder in Cross Flow". In Proceedings of the 8th International Symposium on Turbulence, Heat and Mass Transfer (THMT15).

[27] D'Alessandro, V., Montelpare, S., and Ricci, R., 2016. "Detached-Eddy Simulations of the Flow Over a Cylinder at $Re = 3900$ Using OpenFOAM". *Computer & Fluids,* **136**, pp. 152–169.

[28] Pereira, F., Vaz, G., Eça, L., and Girimaji, S., 2018. "Simulation of the Flow Around a Circular Cylinder at $Re = 3900$ with Partially-Averaged Navier-Stokes Equations". *International Journal of Heat and Fluid Flow,* **69**, pp. 234–246.

[29] Wilcox, D., 1988. "Reassessment of the Scale-Determining Equation for Advanced Turbulence Models". *American Institute of Aeronautics and Astronautics (AIAA) Journal,* **26**(11), pp. 1299–1310.

[30] Menter, F., Kuntz, M., and Langtry, R., 2003. "Ten Years of Industrial Experience with the SST Turbulence Model". In Proceedings of the 4th Turbulence, Heat and Mass Transfer, pp. 625–632.

[31] Kok, J., 2000. "Resolving the Dependence on Freestream Values for the $k - \omega$ Turbulence Model". *American Institute of Aeronautics and Astronautics (AIAA) Journal,* **38**(7), pp. 1292–1295.

[32] Lakshmipathy, S., and Girimaji, S., 2006. "Partially-Averaged Navier-Stokes Method for Tur-

bulent Flows: $k-\omega$ Model Implementation". In Proceedings of the 44th American Institute of Aeronautics and Astronautics (AIAA) Aerospace Sciences Meeting and Exhibit.

[33] Menter, F., 1993. "Zonal Two Equation $k-\omega$ Turbulence Models for Aerodynamic Flows". In Proceedings 24th American Institute of Aeronautics and Astronautics (AIAA) Fluid Dynamics Conference, no. AIAA 93-2906.

[34] Menter, F., 1994. "Two-Equation Eddy-Viscosity Turbulence Models for Engineering Applications". *American Institute of Aeronautics and Astronautics (AIAA) Journal,* **32**(8), pp. 1598–1605.

[35] Pereira, F., Vaz, G., and Eça, L., 2015. "An Assessment of Scale-Resolving Simulation Models for the Flow Around a Circular Cylinder". In Proceedings of the 8th International Symposium on Turbulence, Heat and Mass Transfer (THMT15).

[36] Gritskevich, M., Garbaruk, A., Schütze, J., and Menter, F., 2012. "Development of DDES and IDDES Formulations for the $k-\omega$ Shear Stress Transport Model". *Flow, Turbulence and Combustion,* **88**(3), pp. 431–449.

[37] Pereira, F., 2018. "Towards Predictive Scale-Resolving Simulations of Turbulent External Flows". Phd thesis, Instituto Superior Técnico, Lisbon, Portugal, March.

[38] Zdravkovich, M., 1997. *Flow Around Circular Cylinders. Volume 1: Fundamentals*, first ed. Oxford Science Publications, Oxford, United Kingdom.

[39] Prasad, A., and Williamson, C., 1997. "The Instability of the Shear Layer Separating from a Bluff Body". *Journal of Fluid Mechanics,* **333**, pp. 375–402.

[40] Ong, L., and Wallace, J., 1996. "The Velocity Field of the Turbulent Very Near Wake of a Circular Cylinder". *Experiments in Fluids,* **20**(6), pp. 441–453.

[41] Parnaudeau, P., Carlier, J., Heitz, D., and Lamballais, E., 2008. "Experimental and Numerical Studies of the Flow Over a Circular Cylinder at Reynolds Number 3900". *Physics of Fluids,* **20**, 085101,.

[42] Norberg, C., 2002. "Pressure Distributions Around a Circular Cylinder in Cross-Flow". In Proceedings of the Symposium on Bluff Body Wakes and Vortex-Induced Vibrations - BBVIV-3.

[43] Norberg, C., 2003. “Fluctuating Lift on a Circular Cylinder: Review and New Measurements”. *Journal of Fluids and Structures,* **17**(1), pp. 57–96.

[44] ReFRESCO, 2018. http://www.refresco.org.

[45] Wilcox, D., 2006. *Turbulence Modeling for CFD*, third ed. DCW Industries, La Cañada, United States of America.

[46] Pereira, F., Vaz, G., and Eça, L., 2015. “Flow Past a Circular Cylinder: A Comparison Between RANS and Hybrid Turbulence Models for a Low Reynolds Number”. In Proceedings of the 34th International Conference on Ocean, Offshore and Arctic Engineering (OMAE).

[47] Pereira, F., Ecca, L., and Vaz, G., 2019. “Simulation of Wingtip Vortex Flows with Reynolds-Averaged NavierStokes and Scale-Resolving Simulation Methods”. *American Journal of Aeronautics and Astronautics*.

[48] Breuer, M., 2018. “Effect of Inflow Turbulence on an Airfoil Flow with Laminar Separation Bubble: An LES Study”. *Flow, Turbulence and Combustion,* **101**(2), pp. 433–456.

[49] Norberg, C., 1987. Effects of Reynolds Number and a Low-Intensity Freestream Turbulence on the Flow Around a Circular Cylinder. Technical Report 87/2, Chalmers University of Technology, Gothenburg, Sweden, May.

[50] Rajagopalan, S., and Antonia, R., 2005. “Flow Around a Circular Cylinder - Structure of the Near Wake Shear Layer”. *Experiments in Fluids,* **38**(4), pp. 393–402.

APPENDIX A DERIVATION OF THE PANS CLOSURES

The derivation of the PANS closures analyzed in this work is described in this section [37]. These are the PANS-WX, SST and TNT models. The section starts by introducing the RANS governing equations of the three closures - Section A.1. For the sake of simplicity, these are presented in a general form that is similar to the three models. Then, Section A.2 presents the derivation of the k and ω transport equations of the three PANS closures.

A.1 General Form of the Governing Equations

The governing equations of the $k-\omega$ WX, SST, and TNT RANS closures possess a similar general form,

$$\frac{\partial k_T}{\partial t} + \langle \overline{V_j} \rangle \frac{\partial k_T}{\partial x_j} = P_{k_T} - \beta^* \omega_T k_T + \frac{\partial}{\partial x_j} \left[\left(\nu + \nu_{t_T} \sigma_k \right) \frac{\partial k_T}{\partial x_j} \right] , \tag{18}$$

$$\frac{\partial \omega_T}{\partial t} + \langle \overline{V_j} \rangle \frac{\partial \omega_T}{\partial x_j} = \frac{\alpha}{\nu_{t_T}} P_{k_T} - \beta \omega_T^2 + \frac{\partial}{\partial x_j} \left[\left(\nu + \nu_{t_T} \sigma_\omega \right) \frac{\partial \omega_T}{\partial x_j} \right] + f \frac{1}{\omega_T} \frac{\partial k_T}{\partial x_j} \frac{\partial \omega_T}{\partial x_j} , \tag{19}$$

where the subscript T denotes total (RANS) turbulence quantities, and f is defined as

$$f = \begin{cases} 0 , & (\text{WX}) \\ 2 \left(1 - F_1 \right) \sigma_{\omega_2} , & (\text{SST}) \\ \sigma_d , & (\text{TNT}) \end{cases} . \tag{20}$$

In the case of the TNT model, $\sigma_d = 0.5$ if $\frac{\partial k_T}{\partial x_j}\frac{\partial \omega_T}{\partial x_j} > 0$, otherwise it is zero. The turbulent viscosity is then defined as

$$\nu_{t_T} = \begin{cases} \frac{k_T}{\omega_T}\ , & (\text{WX, TNT}) \\ \\ \frac{a_1 k_T}{\max\left\{a_1\omega_T;\langle\overline{S}\rangle F_2\right\}}\ , & (\text{SST}) \end{cases} . \tag{21}$$

All coefficients and auxiliary functions of these closures have been described in Section 2.

A.2 PANS Closures Governing Equations

As discussed in Section 2, PANS represents the dynamics of the unresolved scales through a RANS-based closure. The original model is therefore modified in order to include parameters that determine the portion of the turbulent dependent variables being modeled. For $k-\omega$ closures, two parameters are required: the modeled-to-total ratio of turbulence kinetic energy f_k and specific dissipation f_ω,

$$f_k \equiv \frac{k}{k_T}, \qquad f_\omega \equiv \frac{\omega}{\omega_T} = \frac{f_\epsilon}{f_k}\ , \tag{22}$$

where f_ϵ is the modeled-to-total ratio of turbulent dissipation,

$$f_\epsilon \equiv \frac{\epsilon}{\epsilon_T}\ . \tag{23}$$

Clearly, the modeled turbulence kinetic energy and dissipation vanish as f_k and f_ϵ tend to zero. At the other extreme, these quantities go to RANS values when f_k and f_ϵ approach unity. The manner how these parameters are included in the original $k-\omega$ WX, SST, and TNT transport equations is now described using the procedure proposed in Girimaji [9].

A.2.1 Transport Equation for Turbulence Kinetic Energy

As demonstrated by Germano [7] and Girimaji [9], equation 18 that represents the transport of total turbulence kinetic energy possesses an averaging-invariant form,

$$\frac{\partial k}{\partial t} + \langle V_j \rangle \frac{\partial k}{\partial x_j} = P_k - \beta^* \omega k + T_k \ , \tag{24}$$

being T_k the transport term. In this manner, the RANS and PANS (constant f_Φ) forms of such transport equation are similar and related according to

$$\frac{\partial k}{\partial t} + \langle \overline{V_j} \rangle \frac{\partial k}{\partial x_j} = f_k \left(\frac{\partial k_T}{\partial t} + \langle \overline{V_j} \rangle \frac{\partial k_T}{\partial x_j} \right) \ , \tag{25}$$

where $\langle \overline{V_j} \rangle$ is the mean-flow velocity vector resultant from a RANS computation. This equation can also be written as

$$\frac{\partial k}{\partial t} + \langle V_j \rangle \frac{\partial k}{\partial x_j} = f_k \left(\frac{\partial k_T}{\partial t} + \langle \overline{V_j} \rangle \frac{\partial k_T}{\partial x_j} \right) + \left(\langle V_j \rangle - \langle \overline{V_j} \rangle \right) \frac{\partial k}{\partial x_j} \ , \tag{26}$$

with the last term representing the contribution of the resolved fluctuating velocity field to the turbulent transport of modeled turbulence kinetic energy. Replacing the material derivative of k_T by the right-hand side of equation 18,

$$\frac{\partial k}{\partial t} + \langle V_j \rangle \frac{\partial k}{\partial x_j} = f_k \left(P_{k_T} - \beta^* k_T \omega_T + \frac{\partial}{\partial x_j} \left[\left(\nu + \nu_{t_T} \sigma_k \right) \frac{\partial k_T}{\partial x_j} \right] \right) + \left(\langle V_j \rangle - \langle \overline{V_j} \rangle \right) \frac{\partial k}{\partial x_j} \ . \tag{27}$$

Applying a similar operation to the left-hand side of equation 27 leads to

$$P_k - \beta^* k\omega + T_k = f_k \left(P_{k_T} - \beta^* k_T \omega_T + \frac{\partial}{\partial x_j} \left[\left(\nu + \nu_{t_T} \sigma_k \right) \frac{\partial k_T}{\partial x_j} \right] \right) + \left(\langle V_j \rangle - \langle \overline{V_j} \rangle \right) \frac{\partial k}{\partial x_j} \, , \tag{28}$$

which demonstrates the similarity between the PANS (left-hand side) and RANS (right-hand side) terms. Using relations 22, it is therefore possible to relate the source/sink terms,

$$P_k - \beta^* k\omega = f_k \left(P_{k_T} - \beta^* k_T \omega_T \right) \Rightarrow P_{k_T} = \frac{1}{f_k} \left(P_k - \beta^* k\omega \right) + \beta^* \frac{k\omega}{f_k f_\omega} \, , \tag{29}$$

and transport terms,

$$T_k = f_k \frac{\partial}{\partial x_j} \left[\left(\nu + \nu_{t_T} \sigma_k \right) \frac{\partial k_T}{\partial x_j} \right] + \left(\langle V_j \rangle - \langle \overline{V_j} \rangle \right) \frac{\partial k}{\partial x_j} \, . \tag{30}$$

Note that the last term of equation 30 is difficult to compute during a simulation and so requires further modeling. The present derivation relies on a approach named zero transport model [9] which neglects this term by assuming that the resolved fluctuating velocity field does not contribute to the turbulent transport of the modeled field,

$$\left(\langle V_j \rangle - \langle \overline{V_j} \rangle \right) \frac{\partial k}{\partial x_j} \approx 0 \, . \tag{31}$$

This assumption is based on the argument that the resolved and modeled fluctuating components of the dependent variable possess different length-scales so that they are poorly correlated. This conducts to the final form of the PANS transport equation for the modeled turbulence kinetic en-

ergy,

$$\frac{\partial k}{\partial t} + \langle V_j \rangle \frac{\partial k}{\partial x_j} = P_k - \beta^* k\omega + \frac{\partial}{\partial x_j}\left[\left(\nu + \nu_t \sigma_k \frac{f_\omega}{f_k}\right)\frac{\partial k}{\partial x_j}\right], \tag{32}$$

where $P_k = \nu_t \langle S \rangle^2$, the total and partial turbulent viscosities are related by

$$\nu_{t_T} = \frac{k_T}{\omega_T} = \frac{k}{\omega}\frac{f_\omega}{f_k} = \nu_t \frac{f_\omega}{f_k}, \tag{33}$$

and the coefficients β^* and σ_k are equal to those given in Section 2.

A.2.2 Transport Equation for Turbulent Specific Dissipation

A similar approach is now applied to derive the PANS transport equation for the turbulent specific dissipation. From the relation between the RANS and PANS form of equation 19, we get

$$\frac{\partial \omega}{\partial t} + \langle \overline{V_j} \rangle \frac{\partial \omega}{\partial x_j} = f_\omega \left(\frac{\partial \omega_T}{\partial t} + \langle \overline{V_j} \rangle \frac{\partial \omega_T}{\partial x_j}\right), \tag{34}$$

which can also be written as

$$\frac{\partial \omega}{\partial t} + \langle V_j \rangle \frac{\partial \omega}{\partial x_j} = f_\omega \left(\frac{\partial \omega_T}{\partial t} + \langle \overline{V_j} \rangle \frac{\partial \omega_T}{\partial x_j}\right) + \left(\langle V_j \rangle - \langle \overline{V_j} \rangle\right)\frac{\partial \omega}{\partial x_j}. \tag{35}$$

Then, replacing the material derivative of ω_T by the right-hand side of equation 19, and using once again the zero transport model leads to

$$\frac{\partial \omega}{\partial t} + \langle V_j \rangle \frac{\partial \omega}{\partial x_j} = f_\omega \left(\frac{\alpha}{\nu_{t_T}} P_{k_T} - \beta \omega_T^2 + \frac{\partial}{\partial x_j}\left[\left(\nu + \nu_{t_T}\sigma_\omega\right)\frac{\partial \omega_T}{\partial x_j}\right] + f \frac{1}{\omega_T}\frac{\partial k_T}{\partial x_j}\frac{\partial \omega_T}{\partial x_j}\right). \tag{36}$$

The PANS form of the ω-equation is finally obtained by introducing relations 22, 29, and 33 in the previous equation,

$$\frac{\partial \omega}{\partial t} + \langle V_j \rangle \frac{\partial \omega}{\partial x_j} = \frac{\alpha}{\nu_t} P_k - \left(P' - \frac{P'}{f_\omega} + \frac{\beta \omega}{f_\omega} \right) \omega + \frac{\partial}{\partial x_j} \left[\left(\nu + \nu_t \sigma_\omega \frac{f_\omega}{f_k} \right) \frac{\partial \omega}{\partial x_j} \right] + f \frac{1}{\omega} \frac{f_\omega}{f_k} \frac{\partial k}{\partial x_j} \frac{\partial \omega}{\partial x_j} \ , \tag{37}$$

where $P' = \alpha \beta^* k / \nu_t$, and the coefficients α, β, and σ_ω are defined in table 1.

LIST OF FIGURES

LIST OF TABLES

FIGURES

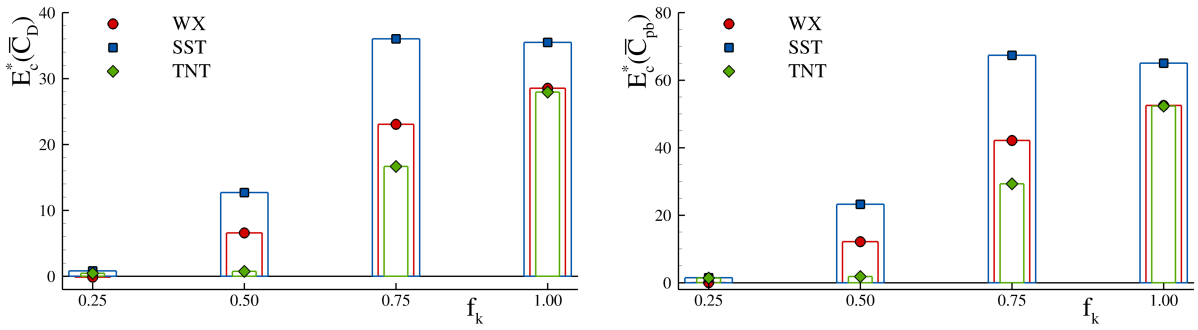

(a) $E_c^*(\overline{C}_D)$ (b) $E_c^*(\overline{C}_{pb})$

Fig. 1: Convergence of the comparison error of the time-averaged drag coefficient $E_c^*(\overline{C}_D)$ and base pressure coefficient $E_c^*(\overline{C}_{pb})$ with the physical resolution f_k for different closures. The symbol $*$ indicates that the comparison error is computed and shown as percentage of the PANS-SST solution at $f_k = 0.15$

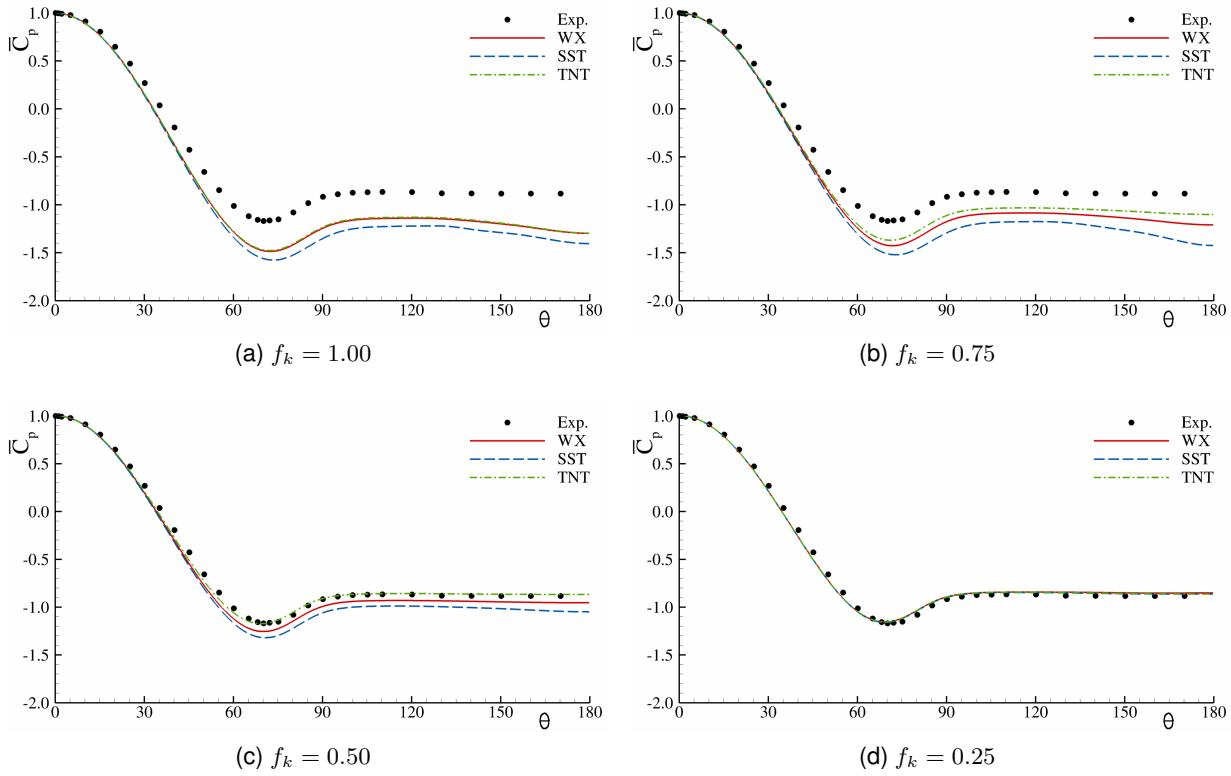

(a) $f_k = 1.00$ (b) $f_k = 0.75$

(c) $f_k = 0.50$ (d) $f_k = 0.25$

Fig. 2: Time-averaged pressure coefficient on the cylinder surface $\overline{C}_p(\theta)$ as a function of the closure and physical resolution f_k. Experimental measurements from Norberg [42]

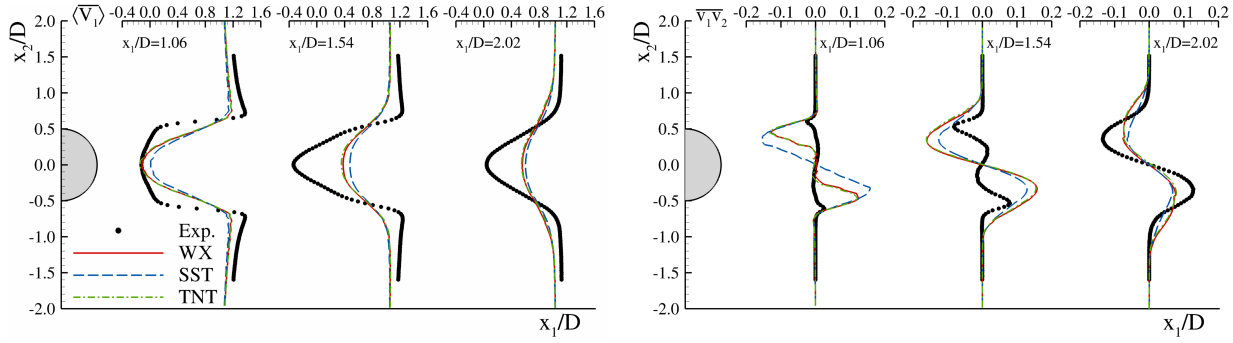

(a) $\langle \overline{V_1} \rangle$ - $f_k = 1.00$

(b) $\overline{v_1 v_2}$ - $f_k = 1.00$

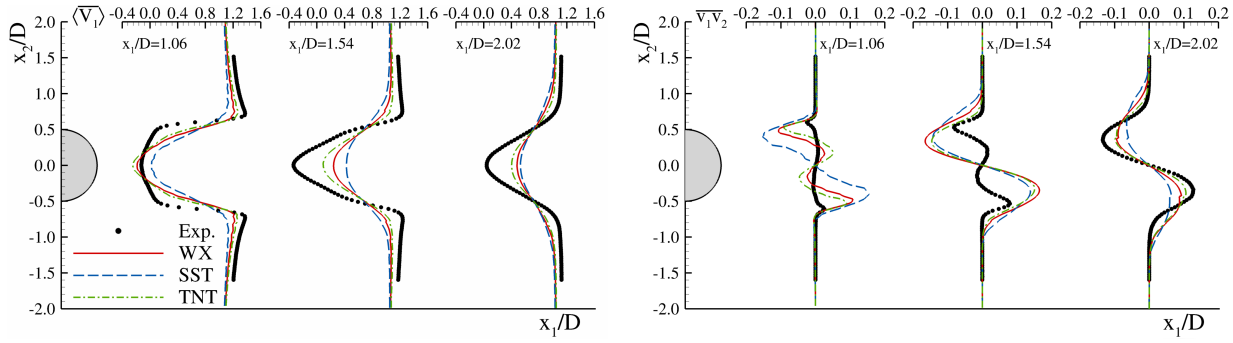

(c) $\langle \overline{V_1} \rangle$ - $f_k = 0.75$

(d) $\overline{v_1 v_2}$ - $f_k = 0.75$

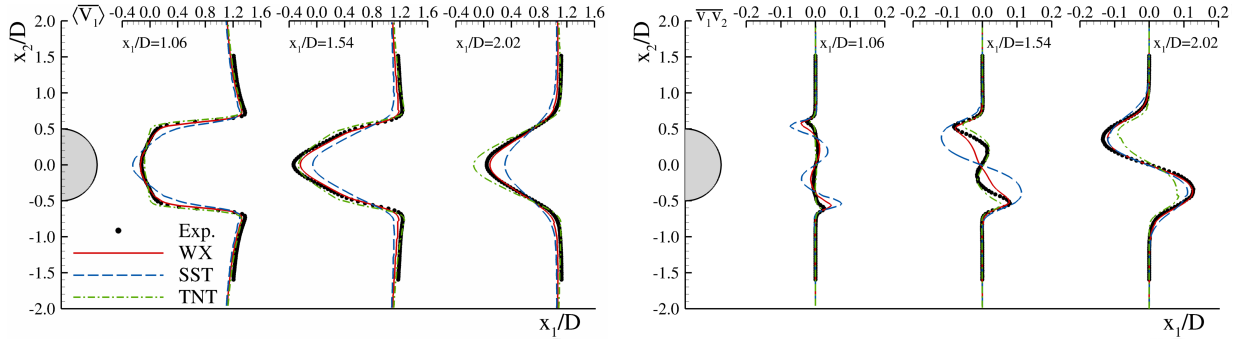

(e) $\langle \overline{V_1} \rangle$ - $f_k = 0.50$

(f) $\overline{v_1 v_2}$ - $f_k = 0.50$

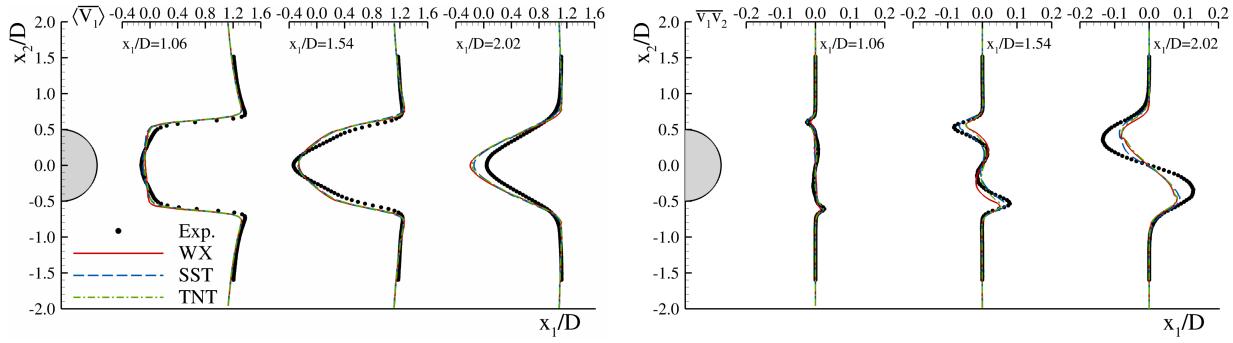

(g) $\langle \overline{V_1} \rangle$ - $f_k = 0.25$

(h) $\overline{v_1 v_2}$ - $f_k = 0.25$

Fig. 3: Time-averaged streamwise velocity magnitude $\langle \overline{V_1} \rangle$ and covariance $\overline{v_1 v_2}$ as a function of the closure and physical resolution f_k. Experimental measurements from Parnaudeau et al. [41]

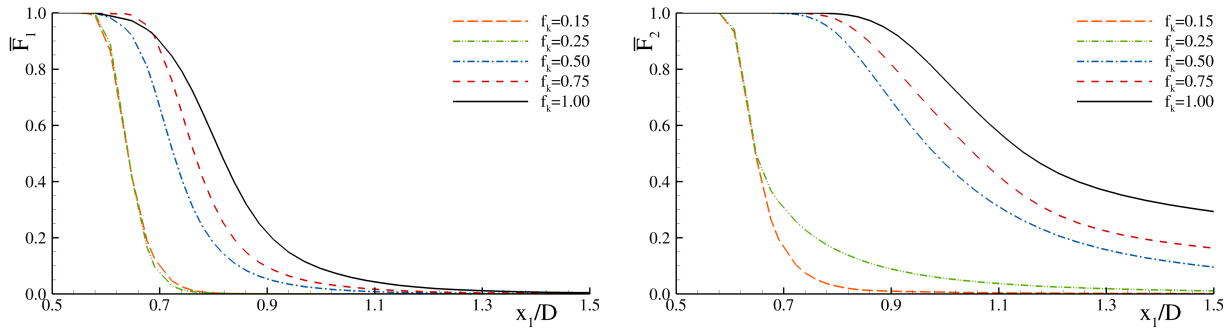

(a) $\overline{F}_1$ (b) $\overline{F}_2$

Fig. 4: Time-averaged PANS-SST auxiliary functions $\overline{F}_1$ and $\overline{F}_2$ along the centerline $x_2/D = 0$ as a function of the physical resolution f_k

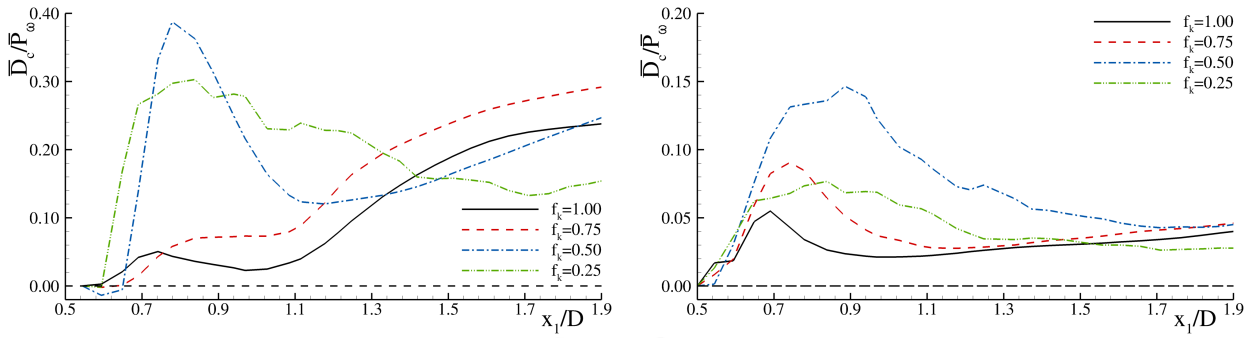

(a) SST (b) TNT

Fig. 5: Time-averaged ratio between the cross-diffusion and specific dissipation production terms $\overline{D}_c/\overline{P}_\omega$ ($\overline{P}_\omega = \alpha \overline{P}_k/\overline{\nu}_t$) as a function of the closure and physical resolution f_k

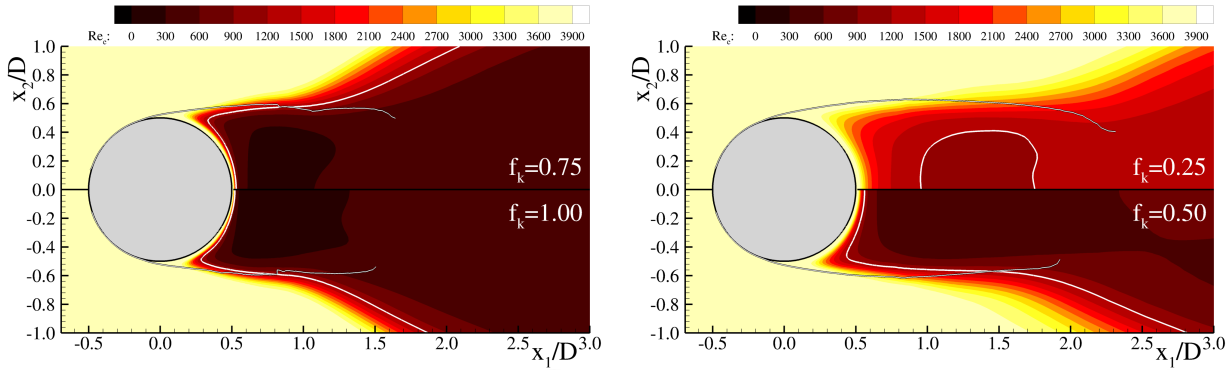

(a) WX - $f_k = 1.00$ and 0.75

(b) WX - $f_k = 0.50$ and 0.25

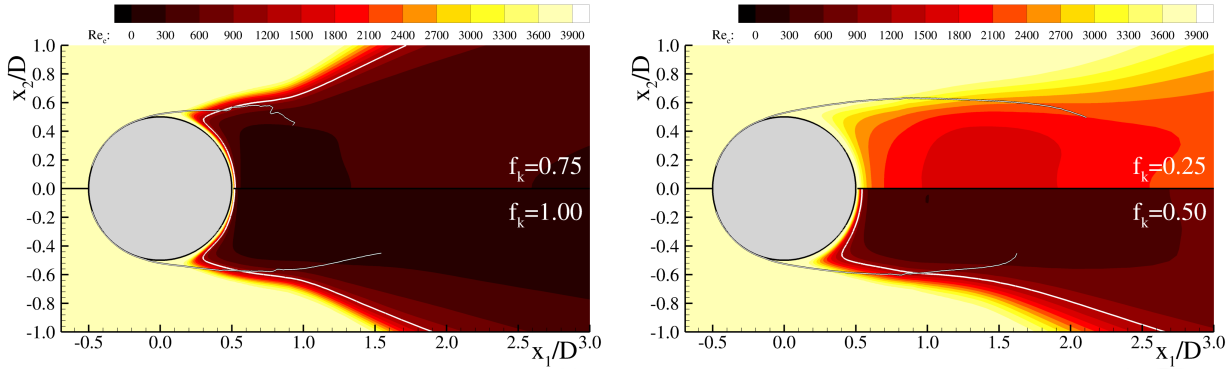

(c) SST - $f_k = 1.00$ and 0.75

(d) SST - $f_k = 0.50$ and 0.25

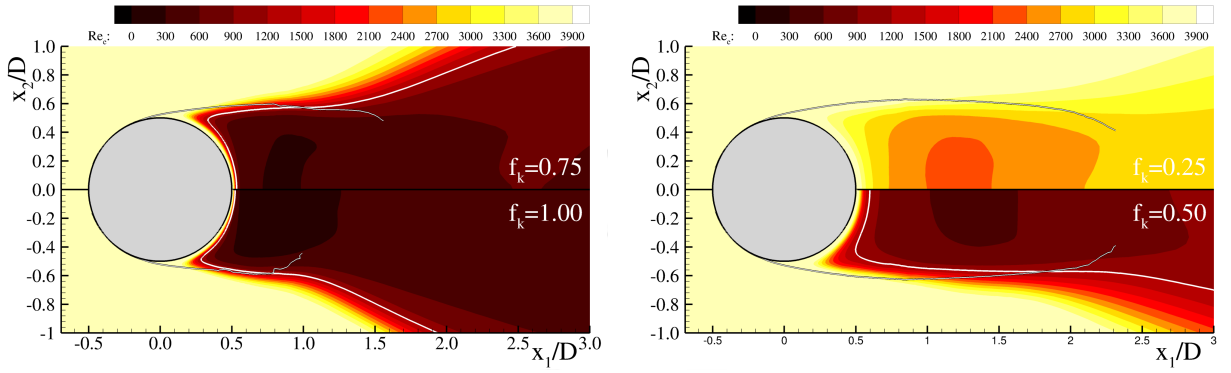

(e) TNT - $f_k = 1.00$ and 0.75

(f) TNT - $f_k = 0.50$ and 0.25

Fig. 6: Time-averaged effective computational Reynolds number Re_e as a function of the closure and physical resolution f_k. White/black lines represent the streamwise velocity inflection point, $\partial^2\langle\overline{V_1}\rangle/\partial x_2^2$, while white lines delimit $Re_e = 1200$

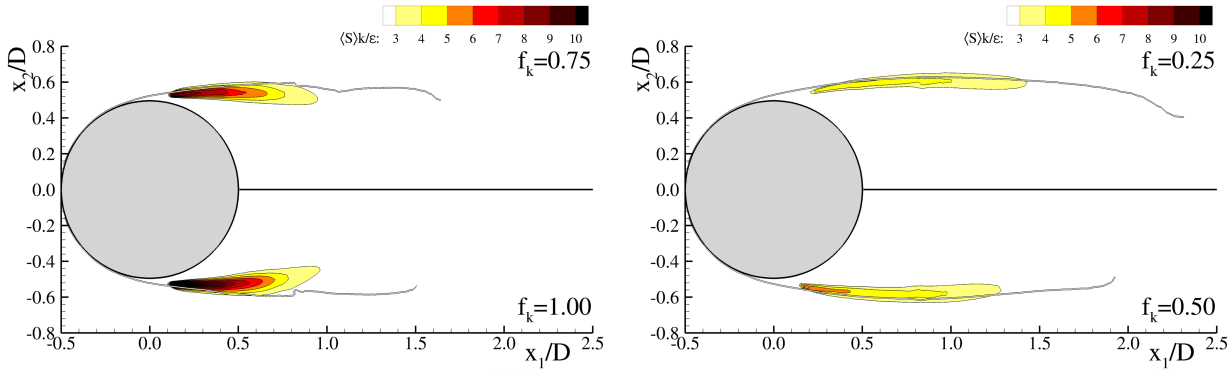

(a) WX - $f_k = 1.00$ and 0.75

(b) WX - $f_k = 0.50$ and 0.25

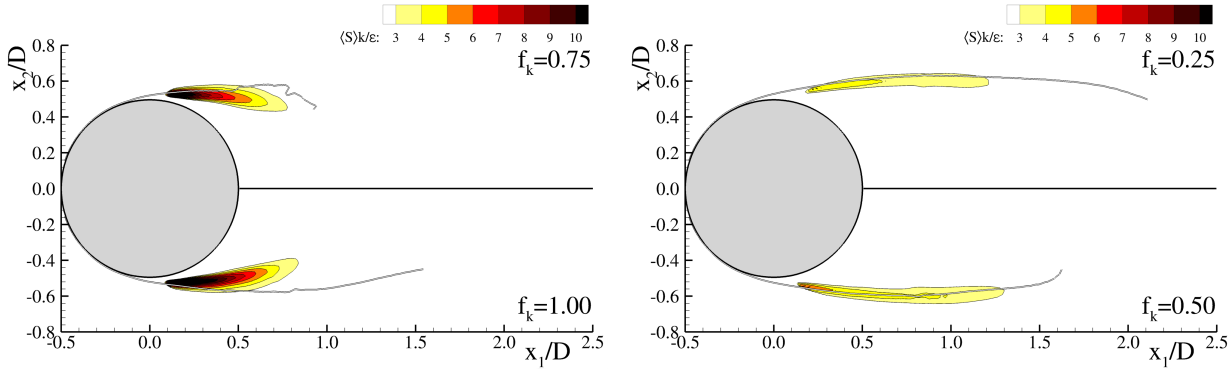

(c) SST - $f_k = 1.00$ and 0.75

(d) SST - $f_k = 0.50$ and 0.25

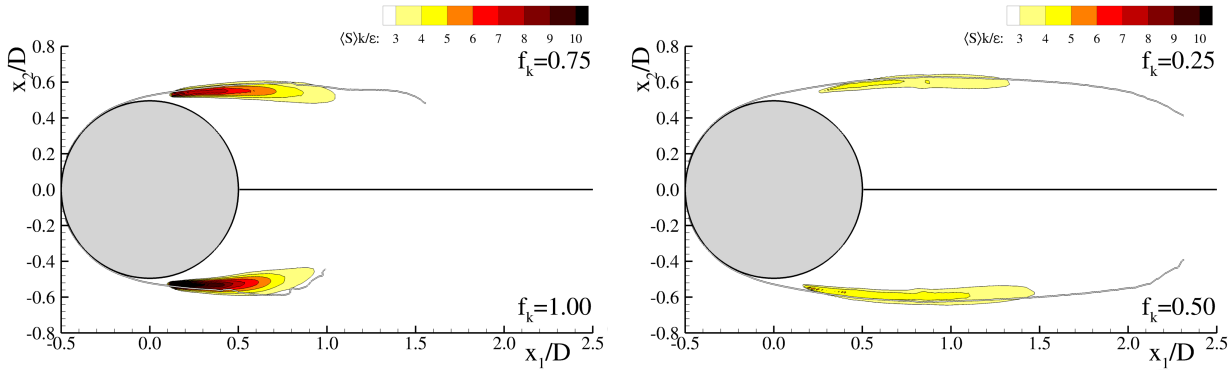

(e) TNT - $f_k = 1.00$ and 0.75

(f) TNT - $f_k = 0.50$ and 0.25

Fig. 7: Time-averaged mean-to-unresolved strain-rate ratio $\langle S \rangle k/\epsilon$ as a function of the closure and physical resolution f_k. White/black lines represent the streamwise velocity inflection point, $\partial^2 \langle \overline{V_1} \rangle / \partial x_2^2$

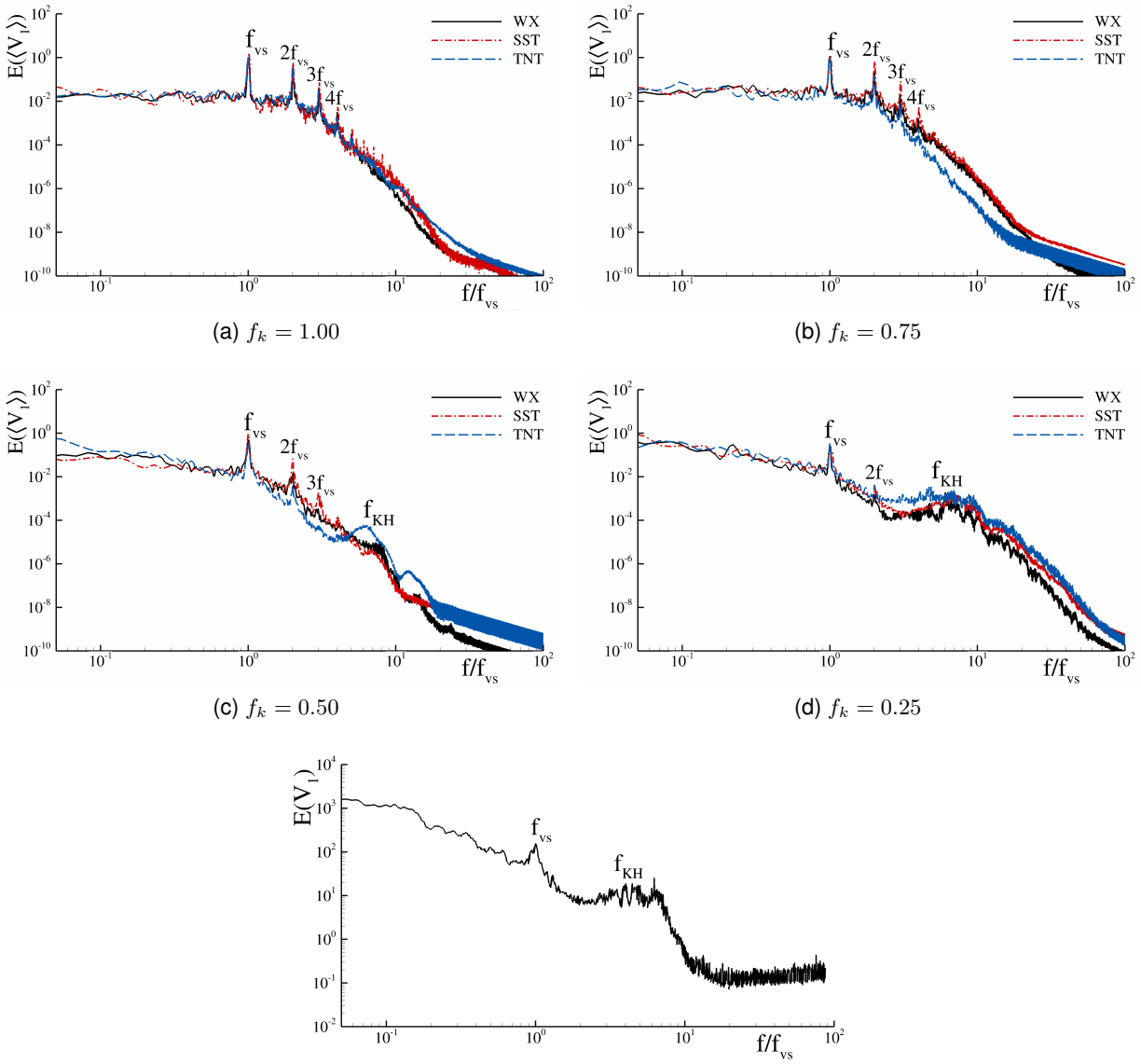

(a) $f_k = 1.00$

(b) $f_k = 0.75$

(c) $f_k = 0.50$

(d) $f_k = 0.25$

(e) Exp.

Fig. 8: Frequency spectrum of the streamwise velocity $E(\langle V_1 \rangle)$ at $\mathbf{x}/D = (0.75; 0.66)$ as a function of the closure and physical resolution f_k. Reference experimental data ($Re = 3700$, and different location) taken from Rajagopalan and Antonia [50]

TABLES

Table 1: Coefficients of the $k-\omega$ PANS closures. Values taken from Wilcox [29], Menter et al. [30], and Kok [31]. Index i only used with the SST closure

Closure	i	α_i	a_1	β_i	β^*	κ	σ_d	σ_{k_i}	σ_{ω_i}
WX	–	$\frac{5}{9}$	–	0.075	0.090	0.410	–	0.500	0.500
SST	1	$\frac{5}{9}$	0.310	0.075	0.090	0.410	–	0.850	0.500
	2	0.440		0.0828			–	1.000	0.856
TNT	–	$\frac{\beta}{\beta^*}-\frac{\sigma_\omega \kappa^2}{\sqrt{\beta^*}}$	–	0.075	0.090	0.410	0.500	$\frac{2}{3}$	0.500

Table 2: Prediction and estimated comparison error $E_c(\Phi)$ of the time-averaged drag coefficient $\overline{C}_D$, root-mean-square lift coefficient C'_L, time-averaged base pressure coefficient $\overline{C}_{pb}$, Strouhal number St, and recirculation length $\overline{L}_r$ as a function of the closure and physical resolution f_k. Comparison error shown as percentage of the experimental data of Parnaudeau et al. [41] and Norberg [42, 43]

	f_k	$\overline{C}_D$		C'_L		$\overline{C}_{pb}$		St		$\overline{L}_r$	
		Φ	$E_c(\Phi)$	Φ	$E_c(\Phi)$	$-\Phi$	$-E_c(\Phi)$	Φ	$E_c(\Phi)$	Φ	$E_c(\Phi)$
WX	1.00	1.18	20.5	0.56	485.9	1.30	47.6	0.214	2.8	0.67	−55.5
	0.75	1.13	15.4	0.46	37.8	1.21	37.6	0.214	2.8	0.81	−46.7
	0.50	0.98	−0.0	0.18	80.7	0.96	8.6	0.214	2.8	1.41	−6.9
	0.25	0.92	−6.3	0.07	−22.1	0.85	−3.2	0.211	1.4	1.77	17.5
SST	1.00	1.25	27.1	0.66	591.8	1.41	59.7	0.211	1.4	0.55	−63.8
	0.75	1.25	27.6	0.67	595.6	1.43	62.0	0.211	1.4	0.53	−64.9
	0.50	1.04	5.7	0.28	195.7	1.05	19.3	0.214	2.8	1.12	−25.6
	0.25	0.93	−5.5	0.10	−1.1	0.86	−1.8	0.208	−0.0	1.73	14.4
	0.15	0.92	−6.2	0.08	−19.9	0.85	−3.2	0.205	−1.4	1.77	17.4
TNT	1.00	1.18	20.0	0.55	474.1	1.30	47.4	0.214	2.8	0.70	−53.6
	0.75	1.07	9.4	0.35	26.9	1.10	25.2	0.214	2.8	0.96	−36.7
	0.50	0.93	−5.5	0.09	−5.1	0.87	−1.4	0.214	2.8	1.70	12.3
	0.25	0.92	−5.8	0.09	−2.7	0.86	−1.9	0.208	−0.0	1.76	16.5
Exp.	–	0.98	–	0.10	–	0.88	–	0.208	–	1.51	–